# Liquid flow and control without solid walls

Peter Dunne[1,2†], Takuji Adachi[1†], Arvind Arun Dev[2], Alessandro Sorrenti[1,3], Lucas Giacchetti[1], Anne Bonnin[4], Catherine Bourdon[5], Pierre Mangin[5], J.M.D. Coey[6], Bernard Doudin[2], Thomas M. Hermans[1,*]

**Affiliations:**

[1] Université de Strasbourg, CNRS, ISIS, 8 allée Gaspard Monge, 67000 Strasbourg, France
[2] Université de Strasbourg, CNRS, IPCMS UMR 7504, 23 rue du Loess, F-67034 Strasbourg, France
[3] Institute for Chemical and Bioengineering, Department of Chemistry and Applied Biosciences, ETH Zürich, Vladimir Prelog Weg 1, 8093 Zürich, Switzerland
[4] Paul Scherrer Institut, CH-5232, Villigen PSI, Switzerland
[5] Université de Strasbourg, INSERM, EFS Grand-Est, BPPS UMR-S 949, FMTS, Strasbourg, F-67000, France
[6] School of Physics and CRANN, Trinity College, Dublin 2, Ireland
[*] Correspondence to: hermans@unistra.fr
[†] Equal contribution

**Solid walls become increasingly important when miniaturizing fluidic circuitry.[1] They limit flow-rates achievable for a given pressure drop, and are plagued by fouling[2]. Approaches to reduce the wall interactions include hydrophobic coatings[3], liquid-infused porous surfaces[4–6], nanoparticle surfactant jamming[7], changing the surface electronic structure[8], electrowetting[9,10], surface tension pinning[11,12], and atomically flat channels[13]. A better solution may be to avoid the solid walls altogether. Droplet microfluidics or sheath flow achieves this, but require continuous flow of both the liquid transported and the outer carrier liquid[1,14]. Here we demonstrate a new approach, where wall-less aqueous liquid channels are surrounded by an immiscible magnetic liquid, both being stabilised by a quadrupolar magnetic field. This creates self-healing, uncloggable, anti-fouling, and near-frictionless liquid-in-liquid fluidic channels with millimetre effective slip lengths. Pumping is achieved by moving permanent magnets that have no physical contact with the liquid channel. We show that this magnetostaltic pumping method can be used to transport whole human blood with very little damage due to shear forces; haemolysis is reduced by an order of magnitude compared to traditional peristaltic pumping. Our liquid-in-liquid approach provides new avenues to transport delicate liquids, particularly when scaling channels down to the micron scale with no need for high pressures, while retaining basic microfluidic circuitry functionalities.**

To avoid contact with the walls of a device, magnetic forces can be used to levitate particles or live cells in a paramagnetic liquid[15]. Furthermore, nearly wall-less microfluidic channels have been demonstrated where continuous 'magnetic antitubes' of water surrounded by an aqueous paramagnetic salt solution are stabilised[16] using an electromagnet and iron tracks. However, the antitube lifetime was limited by ion interdiffusion between the two liquids, the salts were toxic, and contact with one stationary wall containing the track could not be avoided. Here we overcome all these limitations, creating entirely wall-less microfluidic channels consisting of diamagnetic antitubes completely enclosed by immiscible, and in select cases non-toxic paramagnetic fluids.

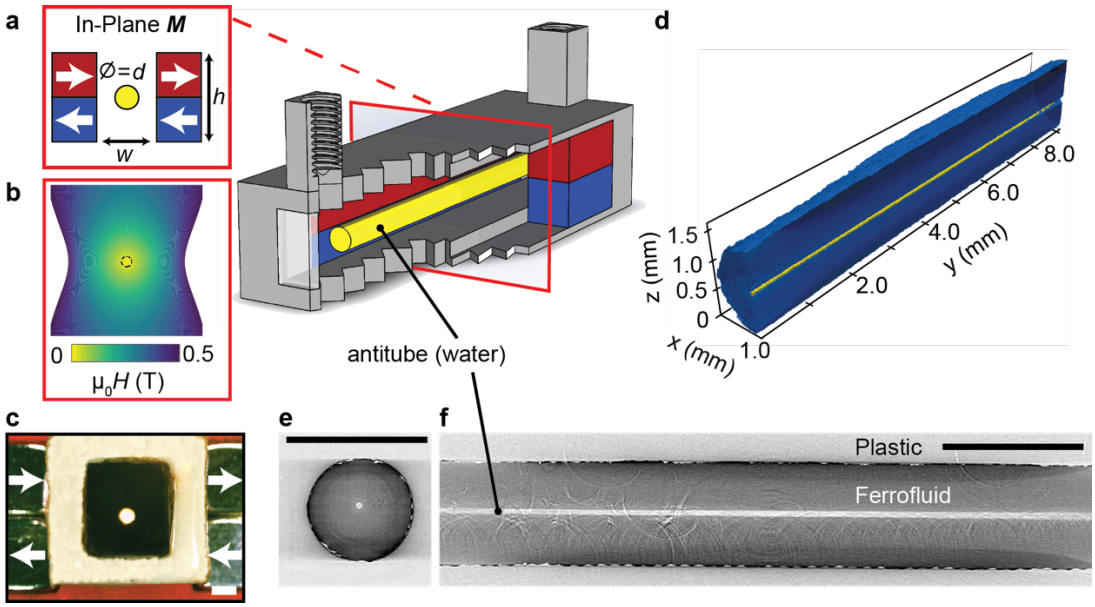


**Fig. 1 | Wall-less magnetic confinement in a fluidic channel.** Centre: exploded view, where permanent magnets (red, blue) in an in-plane quadrupolar configuration create a low-field zone at the centre **a**, where an antitube of water (yellow) is stabilized inside an immiscible magnetic liquid; **b** contour plot of the magnetic field; **c** synchrotron X-ray tomographic reconstruction of a water antitube (yellow) with diameter 81 μm surrounded by ferrofluid (blue); **d** X-ray end-view cross-section from tomographic data at $y$ = 4 mm; and **e** X-ray side-view cross-section from tomographic data at $x$ = 1 mm. Black scale bars are 2 mm.

The key to wall-less magnetic confinement is an extended quadrupolar flux source leading to a null magnetic field along a line at the centre (Fig. 1a,b). Appropriately-magnetised $Nd_2Fe_{14}B$ bars were used to define tubular channels, or else custom-made magnet bilayers were waterjet cut to define more

complex fluidic circuitry. The magnetic bars are housed in 3D-printed supports with conventional microfluidic inlet and outlet ports (Fig. 1, and Fig. E1 in Extended Data). The various magnetic fluids used are listed in Table 1; stronger confinement is achieved with ferrofluids, but optical transparency is possible using 'Magoil'. The former are colloidal liquids of nanometre sized magnetite, $Fe_3O_4$, nanoparticles suspended in a carrier fluid, while the latter is a rare-earth based oil, inspired by the diethylenetriaminepentaacetate-based contrast agents used for magnetic resonance imaging[17] (Fig. E2 and Methods M1, M2). We used commercial ferrofluids from Ferrotec, APG311 and EMG900 1 vol.% and 13 vol.% magnetite in hydrocarbon oils respectively, and from Qfluidics, MKC which is 29 vol.% magnetite in hydrocarbons, and MD4 which is 5 vol.% magnetite in perfluorodecalin.

**Table 1. Characteristics of the magnetic fluids.**

| Magnetic liquid | Susceptibility $\chi$ | Viscosity $\eta$ (mPa s)* | Appearance |
|---|---|---|---|
| **Magoil** | $4.7 \times 10^{-4}$ | 600 | Transparent |
| **APG311 ferrofluid** | 0.085 | 70 | Opaque / black |
| **EMG900 ferrofluid** | 1.67 | 60 | Opaque / black |
| **MKC ferrofluid** | 1.88 | 380 | Opaque / black |
| **MD4 ferrofluid** | 0.315 | 180 | Opaque / black |

*at a shear rate of 100 $s^{-1}$

Aqueous antitubes were typically formed by injecting ferrofluid into water-filled quadrupole channels and visualised by X-ray imaging & tomography (Fig. 1c–e). Tomography images unambiguously reveal the wall-less features, confirmed by visual inspection of transparency of a tubular shape on antitubes up to 1 m long (Fig. E1g). Optical imaging was found possible through no more than 200 μm thick ferrofluid and a high contrast camera (Fig. E7c-g), where we can take advantage of the optical resolution to image the smallest antitube features. Antitubes in transparent Magoil could be imaged using standard optical or fluorescent microscopy by adding contrast ink or fluorescent dye to the water antitube, allowing real-time visualisation of antitube extrusion and retraction (video 1). Furthermore, trapped gas bubbles that are often problematic in conventional devices can easily be

removed, since their buoyancy in Magoil overcomes the magnetic confinement. For most practical applications, however, ferrofluids are preferred because of their much larger magnetic susceptibility $\chi$ (Table 1); they can withstand significant flow rates while remaining confined in the quadrupole (Fig. E3 a,b) – a 1 mm diameter liquid tube can deliver ~ 40 mL/min flow. In addition, the phase transfer of magnetite nanoparticles into water is very low, with measured iron concentrations mostly below a part per million (Methods M14).

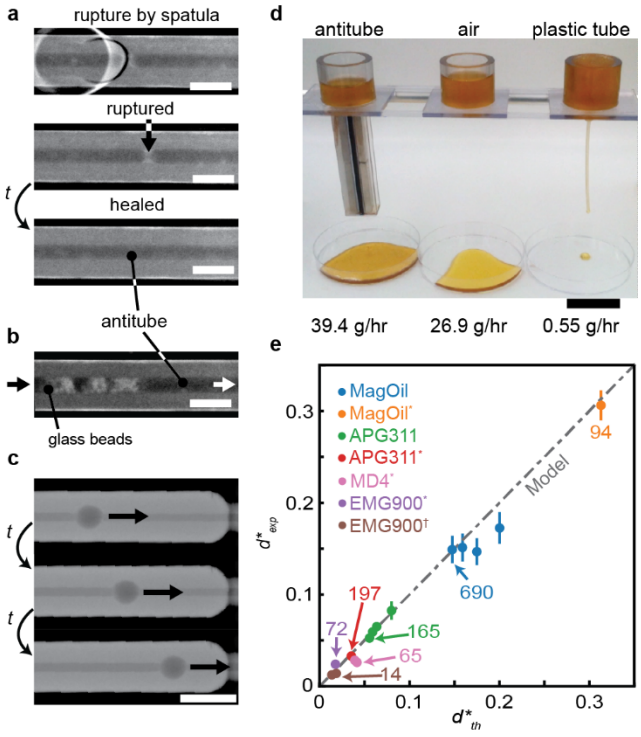


**Fig. 2 | Unique properties and scaling of water antitubes. a** Top-view X-ray images illustrating the mechanical rupture of a tube using a spatula, followed by self-healing, returning to equilibrium within minutes; **b** 0.6 mm glass beads inserted into a 1.5 mm antitube that can be expelled with a slight increase in applied pressure; **c** a 2 mm diameter bead larger than the antitube diameter ($d$ = 0.5 mm) does not cause clogging; there is only a small increase in flow rate after the bead is expelled; **d** comparative flow of honey under gravity (see video 4) through an antitube (left), a normal tube of the same diameter (right) and free fall (centre). Scale bar is 4 cm. **e** plot of experimental dimensionless antitube diameters $d^* = d/w$ ($w$ the spacing between the magnets) versus theoretical values calculated from Eqn. 4, for a series of magnetic fluids. Numbers indicate the smallest tube diameters in

μm, and * denotes water containing 1 vol.% Tween-20, while † denotes 1 vol.% Span-80 in the ferrofluid in addition to 1 vol.% Tween-20 in the water.

The liquid-in-liquid design offers advantages of stability and robustness for fluid transport. Fig. 2a illustrates self-healing after an antitube in ferrofluid was severed with a spatula. Recovery without applied external pressure is rapid (self-healing in Magoil is illustrated in video 2). The antitubes cannot clog: when glass beads are introduced (Fig. 2b), they are easily flushed out. Even a bead much larger than the antitube diameter can be pushed through using minimal pressure (20 mbar, Fig. 2c). The liquid walls of the antitube stretch to avoid clogging and return to their original size when the obstruction is expelled. A change of external pressure alters the antitube size. In Fig. E3 c,d it can be seen that antitubes remain unchanged with externally applied pressure for an open outlet at atmospheric pressure, but dilate when the same pressure is applied with the outlet closed off. This can also be seen in Fig. 2c where the tube dilates behind the bead to accommodate the increased local pressure. As a demonstration of anti-fouling behaviour, we covalently crosslinked a photoresist inside an antitube, and were able to remove the solid polymer rod from the outlet of the device (Fig. E4 and video 3).

A further advantage of liquid-in-liquid flow is near-frictionless transport with negligible pressure drop. A dramatic illustration is shown in Fig. 2d and video 4, where flow of a magnetically confined antitube made of honey (dynamic viscosity $\eta_h$ = 10 Pa.s) is compared to honey flow in a standard tube. Here, we observed an antitube flow of 39.4 ± 0.7 g/hour, ~70 times faster than the flow through a conventional plastic tube of the same diameter $d$ = 1.1 mm, (0.55 ± 0.10 g/hour). The ferrofluid acts as a lubricating layer, with an effective slip length $b$ at the honey/ferrofluid boundary that can be approximated by (SI section 1)

$$b = \frac{1}{2}\left[\sqrt{\frac{d^2}{2}\left(Q_{ND}+1\right)} - d\right] \tag{1}$$

where $d$ is the antitube diameter and $Q_{ND}$ is the non-dimensional flow rate given by

$$Q_{ND} = \frac{128 Q \eta_h}{\pi d^4 \, \partial P/\partial z} \tag{2}$$

Where $Q$ is the flow rate, and $\partial P/\partial z$ is the pressure gradient in the flow direction. Experimentally, we obtain an effective slip length of 4.3 mm, meaning the flow is essentially plug-like. Under the assumption of an infinite channel, the plug-like velocity profile can be calculated, as shown in Fig. E3 e.f., leading to a theoretical effective slip length of 8.1 mm. Remarkably, the flow rate of honey through the antitube was 1.5 times faster than when it fell freely and unconfined, likely due to competition between orifice wetting[18] and the higher hydrostatic pressure due to the greater height of the honey column in the antitube design.

The stable confinement of an antitube, at equilibrium, results from the competing magnetic energy of the confining fluid and the surface energy $\sigma$ of the magnetic/non-magnetic interface. These two energy densities, or effective pressures, inserted into the magnetically augmented version of Bernoulli's equation[19], give the equilibrium diameter of the antitube, derived in supplementary information (SI) S2:

$$d = \frac{4\sigma}{2\mu_0 \overline{M} H_I + \mu_0 M_I^2} \tag{3}$$

where $H_I$, $M_I$ are the magnetic field and magnetization values at the interface, $\mu_0$ is the permeability of free space, and $\overline{M}$ is the field-averaged magnetization of the confining fluid induced by $H_I$. This equation is valid when the magnetic pressure, $\frac{1}{2}\mu_0 H^2$ is significantly larger than any difference in hydrostatic pressure. It can then be linearized when $M = \chi H$, under the geometrical conditions $w \leq \frac{1}{2} h$, and $d \leq \frac{1}{2} w$, typical of our devices, where $w$ is the spacing between the magnets. The linear model (LM) gives the minimum equilibrium dimensionless diameter $d^* = d/w$ as:

$$d^* = \sqrt[3]{\frac{\pi^2}{N_D \chi(\chi+1)}} \tag{4}$$

where $N_D = \frac{\mu_0 M_r^2 w}{\sigma}$ is the magnetic confinement number expressing the ratio of magnetic to surface energies (SI, section 3), and $M_r$ is the remnant magnetisation of the permanent magnets. Note that a

1000-fold increase in $\chi$ reduces $d^*$ by a factor 100, revealing the importance of the magnetic susceptibility of the confining fluid.

We have studied how the attainable antitube diameters vary with $w$ for the paramagnetic confinement liquids of Table 1. There is good agreement between the experimental points for water antitubes and the predictions of Eqns. (3) and (4), using measured susceptibility $\chi$ and interface energy $\sigma$ (Table E1). The addition of a surfactant to the water phase, the magnetic fluid phase or to both[20], leads to smaller antitubes since $\sigma$ is lowered; 1 vol.% or 23 mM Span-80, in the ferrofluid, and 1 vol.% or 0.58 mM Tween-20 in the aqueous antitube. Although the critical micelle concentrations of Span-80 and Tween-20 in water-hydrocarbon interfaces are 1.2 mM and 0.58 mM, respectively[21], we did not observe surfactant-induced structure formation. The close agreement is shown in the plot of dimensionless diameters $d^*$ in Fig. 2e where a plot of the experimental values versus predicted diameters collapse onto one curve for all ferrofluids, surface tensions, and magnet gaps used. The smallest antitube that could be detected so far has $d = 14 \pm 2$ μm, using a strong ferrofluid, EMG900 (Fig. E7). Our model predicts that antitubes below 1 μm can be stabilised, even with a 100 μm sized magnet spacing using a strong ferrofluid (MKC), but they are currently below the detection limit of our imaging methods.

Magnetic confinement can be used to implement basic microfluidic operations. In order to make branched antitube devices we resort to out-of-plane quadrupolar fields, made by waterjet cutting two stacked $Nd_2Fe_{14}B$ plates (Fig. 3a). The null-field line follows the channel centre independently of the channel angle with respect to the magnets, which is not the case for in-plane quadrupoles. Symmetric splitting of the flow was demonstrated in a ferrofluid antitube Y-junction (video 7). Merging of the flow at a Y-junction was visualized using antitubes stabilized by Magoil. Remarkably, merging and rapid mixing occurs immediately after a Y-junction (Fig. 3b), similar to mixing in magnetically-stabilised aqueous paramagnetic tubes surrounded by water[16]. This behaviour is in contrast to the laminar flow observed in a 3D printed microfluidic chip with the same channel size and geometry as the antitube (Fig. 3c).

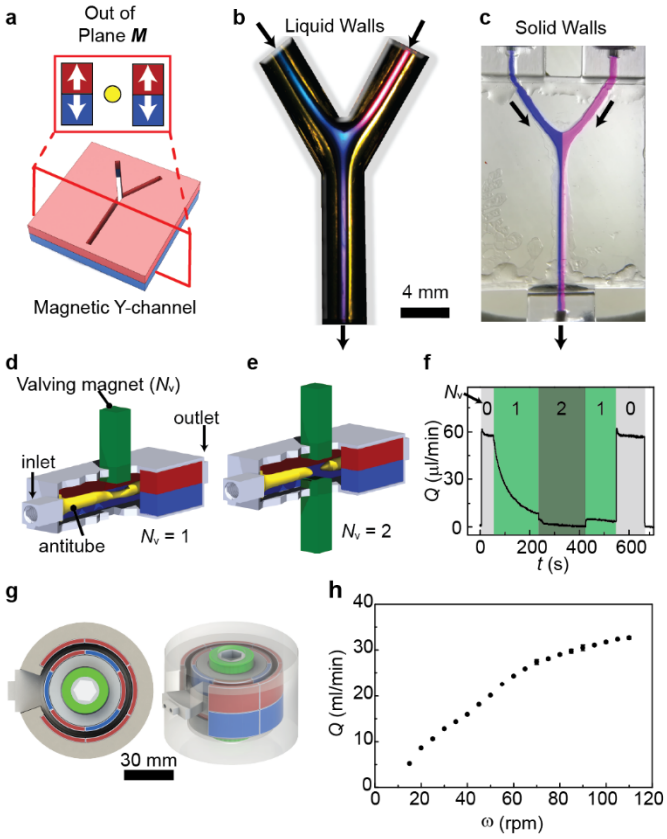


**Fig. 3 | Magnetically implemented mixing, valving and pumping fluidic functionalities.** **a** Out of plane magnetization configuration for a Y-junction cut in a double magnet sheet; **b** optical image of a $Tb^{3+}$–Magoil stabilised aqueous antitube, where blue and pink dye are introduced at the inlets (300 µL $min^{-1}$), and mix immediately upon contact before flowing to the outlet; **c** comparison with normal microfluidic channels, where no mixing is observed: **d** valving with one magnet ($N_v$ = 1, video 9) or **e** two magnets ($N_v$ = 2, video 10); **f** measured flow rate at the exit port controlled by 1 or 2 valving magnets; **g** top-view and isometric-view of a magnetostaltic Qpump with rotating magnetic segments. The orientation of magnetization for the arc segments is radially outward (red) or inward (blue); **h** average flow rate, $Q$ vs rotation rate ω of the inner rotor.

As our microfluidic circuits are magnetically defined, we can exploit the fact that structured magnetic fields can be modulated by mechanical or electrical means to impose unique and versatile control of fluidic devices. Valves can be constructed by moving one or two longitudinally-magnetised bars towards the quadrupole axis. The valving magnets simply pinch off the antitube by removing the null field at the centre (Fig. 3d, 3e), thus interrupting the liquid flow (see videos 8-10 which plot the 150 mT isovolume surfaces). A single transverse valving magnet was able to sustain an excess pressure of

125 mbar, whereas a dual valve (Fig. 3f) withstood 300 mbar. Pumping is as an extension of the valving principle; travelling pinch points can be created by mechanical displacement of magnets. This can be sequential excitation of electro- or electro-permanent magnets, or a rotating array of magnetic spokes (see Fig. E5a-c). A more sophisticated pump based on radially magnetized arc-segments fixed onto a rotor and stator, and a 3D printed fluidic support is illustrated in Fig. 3g, with magnetic field contours shown in Fig. E5g. This 'Qpump', using MKC ferrofluid, produces pressures of up to 900 mbar and flow rates of 32.7 ± 0.3 mL/min (video 12, Fig 3h).

Since the antitube inside the Qpump has no solid walls, we expected that magnetostaltic pumping would be gentler than peristaltic pumping, where a plastic tube is mechanically squeezed by a roller. It is known that blood pumping results in haemolysis, shear-induced rupture of red blood cells that releases haemoglobin.[22–27] High concentrations of free haemoglobin are cytotoxic, and have been associated with clinical complications including an increased incidence of thrombosis, morbidity, and mortality.[22–27] We therefore compared the effects of pumping 6 mL samples of human donor blood collected on hirudin anticoagulant at 1.5 mL/min for 1h in a closed loop using either the Qpump or a peristaltic pump (Fig. 4c). Haematological parameters such as haematocrit and cell counts of the pumped blood did not show differences between the Qpump and the peristaltic pump (Fig. 4a and Table E3). Moreover, functions of platelets which circulated through the Qpump were unchanged as they responded normally to agonists such as Thrombin receptor-activating peptides (TRAP) in the widely used light transmission aggregation test (Fig 4b). Further inspection of platelet morphology by scanning electron microscopy (SEM) confirmed that platelets were intact and normal after pumping (Fig. E6 a-c). In short, these experiments have revealed no adverse effects of whole blood pumped using the Qpump, as compared to a peristaltic pump (Fig E6d).

In contrast, a large difference was found in the degree of haemolysis (Fig. 4d,e). Platelet rich plasma obtained by centrifugation of whole blood is transparent after pumping using the Qpump, but it is bright red after peristaltic pumping (insets Fig. 4d). Based on the UV-Vis absorbance of haemoglobin[28], the concentration of plasma-free haemoglobin (PFH) was determined to be 130 ± 40

mg/dL and 12 ± 5 mg/dL for the peristaltic pump and Qpump respectively (Fig 4e). The degree of haemolysis is 11 ± 6 times lower for blood pumped by the Qpump versus the traditional peristaltic pump. PFH values greater than 20 mg/dL are indicative of significant haemolysis[29], and previous reports on packed red blood cells transfusion using infusion pumps showed 2–3 orders of magnitude higher PFH values[26,27], which demonstrates that magnetic pumping is a promising way to achieve gentle transportation of blood. This method could be applied to other fragile entities such as antibodies or stem cells.

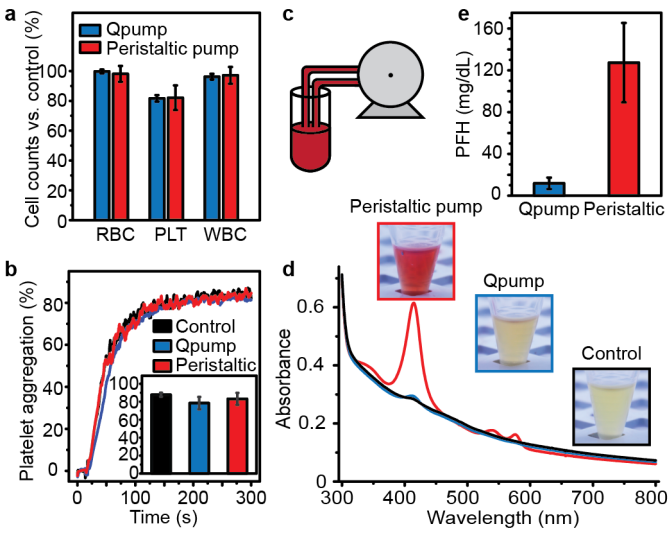


**Fig. 4 | Blood pumping by a magnetostaltic pump.** Blood was circulated in a closed-loop circuit either by the Qpump (filled with 7x diluted MKC ferrofluid) or a normal peristaltic pump. **a** Blood cell counts (RBC: red blood cells, PLT: platelets, WBC: white blood cells) after pumping normalized versus control blood; **b** The degree of platelet aggregation activated by Thrombin receptor-activating peptides (TRAP) tested for PRP from blood after peristaltic pumping and Qpumping compared with control blood. Light transmission is minimal before aggregation as platelets scatter light, but upon addition of TRAP the platelets aggregate and transmission increases; **c** closed-cycle pumping scheme used; **d** Absorption spectrum of platelet rich plasma (PRP) from blood after peristaltic pumping and Qpumping compared with control blood 25 times diluted with phosphate buffer; **e** Plasma-free haemoglobin (PFH) concentration estimated from the absorbance of PRP for Qpump and peristaltic pump.

Our extensive investigations have established that magnetic control of liquid-in-liquid flow opens new possibilities for microfluidics, allowing novel channel shapes and low-pressure cargo transport surpassing the current capabilities of standard microfluidics. We have identified the basic physical quantities controlling the size of confined diamagnetic fluid circuitry, and have given examples of key microfluidic device elements, demonstrating the possibilities of this liquid-in-liquid flow technology. The new method offers low-shear flow and pumping, which is of growing importance in biotechnology where delicate cells, proteins, and antibodies are commonly damaged by traditional pumps.[30–34] There is the prospect that low-shear magnetic blood pumping might eventually be implemented in heart-lung machines during cardiopulmonary bypass surgery, or in devices for extra-corporeal membrane oxygenation.[22–25] At a more fundamental level, our findings lead us to envisage miniaturized fluidic circuits without solid walls that will be scalable down to the submicron level. We can then take full advantage of the versatility of magnetic control at the nanoscale to open the door to practical low pressure nanofluidics[35–37].

## References:


1. Tabeling, P. *Introduction to Microfluidics*. (OUP Oxford, 2005).

2. Mukhopadhyay, R. When Microfluidic Devices Go Bad. *Anal. Chem.* **77**, 429 A-432 A (2005).

3. Zhao, B., Moore, J. S. & Beebe, D. J. Surface-Directed Liquid Flow Inside Microchannels. *Science* **291**, 1023–1026 (2001).

4. Wong, T.-S. *et al.* Bioinspired self-repairing slippery surfaces with pressure-stable omniphobicity. *Nature* **477**, 443–447 (2011).

5. Wang, W. *et al.* Multifunctional ferrofluid-infused surfaces with reconfigurable multiscale topography. *Nature* **559**, 77 (2018).

6. Leslie, D. C. *et al.* A bioinspired omniphobic surface coating on medical devices prevents thrombosis and biofouling. *Nat. Biotechnol.* **32**, 1134–1140 (2014).

7. Forth, J. *et al.* Reconfigurable Printed Liquids. *Adv. Mater.* 1707603 (2018). doi:10.1002/adma.201707603

8. Secchi, E. *et al.* Massive radius-dependent flow slippage in carbon nanotubes. *Nature* **537**, 210–213 (2016).

9. Banerjee, A., Kreit, E., Liu, Y., Heikenfeld, J. & Papautsky, I. Reconfigurable virtual electrowetting channels. *Lab. Chip* **12**, 758 (2012).

10. Choi, K., Ng, A. H. C., Fobel, R. & Wheeler, A. R. Digital Microfluidics. *Annu. Rev. Anal. Chem.* **5**, 413–440 (2012).

11. Lee, W. C., Heo, Y. J. & Takeuchi, S. Wall-less liquid pathways formed with three-dimensional microring arrays. *Appl. Phys. Lett.* **101**, 114108 (2012).

12. Walsh, E. J. *et al.* Microfluidics with fluid walls. *Nat. Commun.* **8**, 816 (2017).

13. Keerthi, A. *et al.* Ballistic molecular transport through two-dimensional channels. *Nature* **558**, 420–424 (2018).

14. Shang, L., Cheng, Y. & Zhao, Y. Emerging Droplet Microfluidics. *Chem. Rev.* **117**, 7964–8040 (2017).

15. Zhao, W., Cheng, R., Miller, J. R. & Mao, L. Label-Free Microfluidic Manipulation of Particles and Cells in Magnetic Liquids. *Adv. Funct. Mater.* **26**, 3916–3932 (2016).

16. Coey, J. M. D., Aogaki, R., Byrne, F. & Stamenov, P. Magnetic stabilization and vorticity in submillimeter paramagnetic liquid tubes. *Proc. Natl. Acad. Sci.* **106**, 8811–8817 (2009).

17. Caravan, P., Ellison, J. J., McMurry, T. J. & Lauffer, R. B. Gadolinium(III) Chelates as MRI Contrast Agents: Structure, Dynamics, and Applications. *Chem. Rev.* **99**, 2293–2352 (1999).

18. Ferrand, J., Favreau, L., Joubaud, S. & Freyssingeas, E. Wetting Effect on Torricelli's Law. *Phys. Rev. Lett.* **117**, 248002 (2016).

19. Rosensweig, R. E. *Ferrohydrodynamics*. (Dover Publications, 2014).

20. Posocco, P. *et al.* Interfacial tension of oil/water emulsions with mixed non-ionic surfactants: comparison between experiments and molecular simulations. *RSC Adv.* **6**, 4723–4729 (2016).

21. Owusu Apenten, R. K. & Zhu, Q.-H. Interfacial parameters for selected Spans and Tweens at the hydrocarbon—water interface. *Food Hydrocoll.* **10**, 27–30 (1996).

22. Byrnes, J. *et al.* Hemolysis During Cardiac Extracorporeal Membrane Oxygenation: A Case-Control Comparison of Roller Pumps and Centrifugal Pumps in a Pediatric Population. *ASAIO J.* **57**, 456 (2011).

23. Omar, H. R. *et al.* Plasma Free Hemoglobin Is an Independent Predictor of Mortality among Patients on Extracorporeal Membrane Oxygenation Support. *PLOS ONE* **10**, e0124034 (2015).

24. Dalton, H. J. *et al.* Factors Associated with Bleeding and Thrombosis in Children Receiving Extracorporeal Membrane Oxygenation. *Am. J. Respir. Crit. Care Med.* **196**, 762–771 (2017).

25. Valladolid, C., Yee, A. & Cruz, M. A. von Willebrand Factor, Free Hemoglobin and Thrombosis in ECMO. *Front. Med.* **5**, (2018).

26. Wilson, A. M. M. M. *et al.* Hemolysis risk after packed red blood cells transfusion with infusion pumps. *Rev. Lat. Am. Enfermagem* **26**, (2018).

27. Hughes, J. *et al.* Infusion Pump-Mediated Mechanical Hemolysis in Pediatric Patients. *Ann. Clin. Lab. Sci.* **45**, 140–147 (2015).

28. Prahl, S. *Optical absorption of hemoglobin*. (Oregon Medical Laser Center, 1999).

29. Baskin, L., Dias, V., Chin, A., Abdullah, A. & Naugler, C. Chapter 3 - Effect of Patient Preparation, Specimen Collection, Anticoagulants, and Preservatives on Laboratory Test Results. in *Accurate Results in the Clinical Laboratory* (eds. Dasgupta, A. & Sepulveda, J. L.) 19–34 (Elsevier, 2013).

30. Jaouen, P., Vandanjon, L. & Quéméneur, F. The shear stress of microalgal cell suspensions (Tetraselmis suecica) in tangential flow filtration systems: the role of pumps. *Bioresour. Technol.* **68**, 149–154 (1999).

31. Kamaraju, H., Wetzel, K. & Kelly, W. J. Modeling shear-induced CHO cell damage in a rotary positive displacement pump. *Biotechnol. Prog.* **26**, 1606–1615 (2010).

32. Vázquez-Rey, M. & Lang, D. A. Aggregates in monoclonal antibody manufacturing processes. *Biotechnol. Bioeng.* **108**, 1494–1508 (2011).

33. Wang, S. *et al.* Shear contributions to cell culture performance and product recovery in ATF and TFF perfusion systems. *J. Biotechnol.* **246**, 52–60 (2017).

34. Nesta, D. *et al.* Aggregation from Shear Stress and Surface Interaction: Molecule-Specific or Universal Phenomenon? *BioProcess International* (2017).

35. Eijkel, J. C. T. & Berg, A. van den. Nanofluidics: what is it and what can we expect from it? *Microfluid. Nanofluidics* **1**, 249–267 (2005).

36. Bocquet, L. & Charlaix, E. Nanofluidics, from bulk to interfaces. *Chem Soc Rev* **39**, 1073–1095 (2010).

37. Bocquet, L. & Tabeling, P. Physics and technological aspects of nanofluidics. *Lab. Chip* **14**, 3143–3158 (2014).

38. Evans, D. F. The determination of the paramagnetic susceptibility of substances in solution by nuclear magnetic resonance. *J. Chem. Soc.* 2003–2005 (1959).

39. Coey, J. M. D. *Magnetism and Magnetic Materials*. (Cambridge University Press, 2010).

40. Sastri, V. R., Perumareddi, J. R., Rao, V. R., Rayudu, G. V. S. & Bünzli, J.-C. G. *Modern Aspects of Rare Earths and their Complexes*. (Elsevier, 2003).

41. Cugat, O., Byrne, R., McCaulay, J. & Coey, J. M. D. A compact vibrating- sample magnetometer with variable permanent magnet flux source. *Rev. Sci. Instrum.* **65**, 3570–3573 (1994).

42. Wysin, G. M. *Demagnetization fields*. (Kansas State University, 2012). https://www.phys.k-state.edu/personal/wysin/notes/demag.pdf

43. Furlani, E. P. *Permanent Magnet and Electromechanical Devices*. (Academic Press, 2001).

44. Schindelin, J. *et al.* Fiji: an open-source platform for biological-image analysis. *Nat. Methods* **9**, 676–682 (2012).

45. Daerr, A. & Mogne, A. Pendent_Drop: An ImageJ Plugin to Measure the Surface Tension from an Image of a Pendent Drop. *J. Open Res. Softw.* **4**, (2016).

46. Marone, F. & Stampanoni, M. Regridding reconstruction algorithm for real-time tomographic imaging. *J. Synchrotron Radiat.* **19**, 1029–1037 (2012).

**Supplementary Information** is linked to the online version of the paper at www.nature.com/nature.

**Acknowledgments:** We acknowledge the support of the University of Strasbourg Institute for Advanced Studies (USIAS) Fellowship, The 'Chaire Gutenberg' of the Région Alsace (J.M.D.C.), the Labex NIE 11-LABX-0058_NIE within the Investissement d'Avenir program ANR-10-IDEX-0002-02, and SATT Conectus funding. This project has received funding from the European Union's Horizon 2020 research and innovation programme under the Marie Skłodowska-Curie grant agreement No 766007. We acknowledge the Paul Scherrer Institut, Villigen, Switzerland for provision of synchrotron radiation beamtime at beamline TOMCAT of the SLS. We are grateful to Dr. Hu Boping, of San Huan Corporation for giving us thin magnetic bilayer sheets. We thank Fabien Chevrier for technical support, and the staff of the STnano nanofabrication facility for help in sample fabrication. We thank Nina Matoussevitch for the synthesis of ferrofluids.